Effective Stability of Quasi-Satellite Orbits in the Spatial Problem for Phobos Exploration

Chen, Hongru
IMCCE, Observatoire de Paris

Canalias, Elisabet
Centre National d'Etudes Spatiales (CNES)

Hestroffer, Daniel
IMCCE, Observatoire de Paris

Hou, Xiyun
Nanjing University

Effective Stability of Quasi-Satellite Orbits in the Spatial Problem for Phobos Exploration

Hongru Chen*
IMCCE, Observatoire de Paris, 75014 Paris, France
Elisabet Canalias[†]
Centre National d'Etudes Spatiales (CNES), 31400 Toulouse, France
Daniel Hestroffer[‡]
IMCCE, Observatoire de Paris, 75014 Paris, France
and
Xiyun Hou[§]
Nanjing University, 210023 Nanjing, People's Republic of China

The generation of bounded trajectories complying with operational constraints in the complex dynamic environment surrounding Phobos is not an easy task. The vicinity of Phobos is dominated by the gravity field of Mars; consequently, orbiting on a Keplerian orbit about this moon is not feasible. The quasi-satellite orbit (QSO) is a means to orbit Phobos in the sense of relative motion. In particular, the three-dimensional QSO (3D QSO) has been recently suggested as an approach for better meeting mission objectives, such as global mapping. However, the linear stability of QSOs concluded in the simplified three-body model cannot sufficiently ensure a stability domain for operations. In this context, this paper investigates the strategy for designing bounded orbits with desired stability properties and characteristics for observation. Families of periodic 3D QSOs are first computed in the circular-restricted three-body problem. The sensitivity of the QSOs to the initial epoch and operational errors is analyzed, revealing effective stability levels and region that can guide trajectory and operation design. The stability levels are then validated by a dispersion analysis in the full dynamics. Furthermore, being guided by effective stability, a preliminary attempt to maintain low-altitude and high-inclination QSOs in the full dynamics has proven successful.

I. Introduction

THE Martian moons, Phobos and Deimos, are of scientific interest because of their unknown origin and formation. They could possibly be captured asteroids or be accreted from postimpact debris disc [1,2]. If either moon was a captured carbon- or water-rich asteroid, that may lead to an explanation for the delivery of water to the terrestrial planet zone [3]. Information of Martian moons can lead to further understanding of the early solar system. The Soviet probes Phobos-1 and Phobos-2 have been sent to explore Phobos in the late 1980s [4]. Over the last two decades, Phobos sample-return mission concepts, such as the Phobos-Grant, PHOOTPRINT, and Martian Moons eXploration (MMX), have been intensively studied by space agencies [5–7]. In particular, the MMX mission will be launched in 2024, and scheduled to return samples from Phobos in 2029 [7]. A sample-return mission involves a series of proximity operations around the target, such as global mapping, approaching, descents, and ascents, which generally require science orbits of good observation characteristics and stable (or easily maintainable) "home" orbits. However, due to the dominant gravity field of Mars in the vicinity of Phobos, the sphere of influence of this moon is below its surface. That makes orbiting on a Keplerian orbit around Phobos infeasible. Early in the mission study for Phobos-1 and Phobos-2, the quasi-satellite orbit (QSO) was proposed as a means to orbit around Phobos in the sense of relative motion [8]. The QSO is a result of the three-body dynamics. It appears centered on the secondary body and revolves in the retrograde direction. Dynamics of the planar 1:1 QSO has been intensively studied (e.g., Refs. [9–11]). In addition, the three-dimensional QSO (3D QSO) going significantly away from the orbital plane of Phobos had been previously identified as convenient locations for maximizing the scientific return of a Phobos exploration mission [6,12]. To be specific, 3D QSOs are favorable for global mapping and identifying physical parameters, such as libration amplitude and high-degree gravitational terms, of the target [13,14].

On the other hand, stability of QSO should be deeply understood in order to ensure mission success, given the complexity of the dynamic environment and errors in operations. The QSO generally exhibits linear stability. However, prestudies for the MMX mission and EQUULEUS mission [15] (i.e., employing an Earth–moon near-rectilinear halo orbit as the science orbit to observe meteor impacts on the moon) showed that, when it comes to real operations, it can be more challenging to maintain the QSO in the vicinity of Phobos than to maintain the Earth–Moon halo orbit, which is linearly unstable (private communication with Japan Aerospace Exploration Agency project teams in October 2017). This counterintuitive result motivates a further investigation to bridge the gap between the understanding of orbital stability and operational robustness. The strategy to maintain an orbit is generally to target a baseline bounded orbit, and determined through trial and error. However, if the baseline orbit cannot stay bounded in the presence of modeling and operational errors before the next control, the orbit maintenance operation is likely to fail. Therefore, the degree of orbital stability should be identified. Ikeda et al. [16] and Wiesel [17] have examined the sensitivity of planar QSOs around Phobos to injection errors. This paper further analyzes QSO stability in the spatial problem covering the 3D QSO. In particular, a methodology to classify QSOs into stability classes, which serves for mission and operation planning, is presented.

*Postdoctoral Researcher, 77 Avenue Denfert-Rochereau; also Centre national de la recherche scientifique, Université PSL, Sorbonne Université, Université de Lille; hongru.chen@hotmail.com.

[†]Mission Analysis Engineer, Flight Dynamics Department, 18 Avenue Edouard Belin; elisabet.canalias@cnes.fr.

[‡]Astronomer, 77 Avenue Denfert-Rochereau; also Centre national de la recherche scientifique, Université PSL, Sorbonne Université, Université de Lille; daniel.hestroffer@obspm.fr.

[§]Professor, School of Astronomy and Space Science, 163, Xianlin Avenue; silence@nju.edu.cn.

The paper is organized as follows. Section II presents the commonly used dynamic models and tools with appropriate modifications, concerning computation of resonant periodic orbits and examination of orbital stability. Section III presents the solution map and linear-stability region of 3D QSOs. Section IV further examines orbital stability through sensitivity analyses of the initial epoch and operational errors. In particular, the so-called J2-Elliptic dynamic model is used to examine the sensitivity to the initial epoch in a simple way. Effective stability levels are determined according to the results. In Sec. V, the effective stability of QSOs concluded in low- and mid- fidelity models is verified in the full dynamic model. To be specific, trials for maintaining hyperstable QSOs are conducted, and long-term orbital behaviors are examined by large-scale Monte Carlo simulations.

II.   Background

A.   Circular Restricted Three-Body Problem

The circular restricted three-body problem (CR3BP) assumes that two primary bodies m_1 and m_2 are moving in a circular orbit about their barycenter. The third body is massless compared to the two primaries. The synodic frame (i.e., the origin at the barycenter of the primaries, the z axis aligned with the direction of the angular velocity of the primary system, the x axis in the direction from the primary to the secondary, and the y axis completing the right-handed coordinate system) is chosen to describe the motion of the third body. For convenience, the system is normalized by setting the length unit, LU, to the distance between the two primaries, the mass unit to the combined mass of the two primaries, and the time unit, TU, to the value such that the angular velocity is unity. Let μ denote the ratio of the mass of the secondary m_2 to the total mass. The normalized dimensionless synodic system is depicted in Fig. 1. In this system, the equations of motion of the third body are expressed as

$$\ddot{x} - 2\dot{y} = \partial U/\partial x \qquad \ddot{y} + 2\dot{x} = \partial U/\partial y \qquad \ddot{z} = \partial U/\partial z \quad (1)$$

where U denotes the pseudogravitational potential expressed as

$$U = (x^2 + y^2)/2 + (1 - \mu)/r_1 + \mu/r_2 \qquad (2)$$

where

$$r_1 = \sqrt{(x+\mu)^2 + y^2 + z^2}, \quad r_2 = \sqrt{(x-1+\mu)^2 + y^2 + z^2} \quad (3)$$

To describe the simplified Mars–Phobos system, $LU = 9377.2$ km, $TU = 4387.775$ s, and $\mu = 1.65778 \times 10^{-8}$ are used in this work.

B.   Symmetric Periodic Orbits

Inspection of Eq. (1) shows two symmetries of the system where solutions are symmetric about the x-z plane and the x axis, respectively. The two symmetries can be expressed as

$$(x,y,z,\dot{x},\dot{y},\dot{z},\ddot{x},\ddot{y},\ddot{z},t)^{\mathrm{T}} \leftrightarrow (x,-y,z,-\dot{x},\dot{y},-\dot{z},\ddot{x},-\ddot{y},\ddot{z},-t)^{\mathrm{T}}$$
$$(x,y,z,\dot{x},\dot{y},\dot{z},\ddot{x},\ddot{y},\ddot{z},t)^{\mathrm{T}} \leftrightarrow (x,-y,-z,-\dot{x},\dot{y},\dot{z},\ddot{x},-\ddot{y},-\ddot{z},-t)^{\mathrm{T}} \quad (4)$$
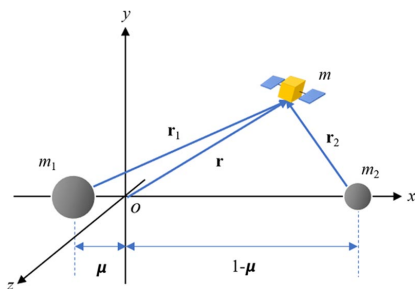

Fig. 1   Dimensionless synodic frame.

If a trajectory perpendicularly crosses the x-z plane or the x axis twice, the trajectory afterward will mirror the trajectory before the last crossing, and thus go back to state at the first crossing, which results in a closed periodic orbit. This property can be used to construct periodic orbits. The periodic orbit that has two perpendicular crossings of the x-z plane is referred to as a *plane-symmetric orbit*, the one that has two perpendicular crossings of the x axis is referred to as an *axi-symmetric orbit*, and the one that has both perpendicular crossings of the x-z plane and x axis is referred to as a *doubly symmetric orbit* [18–20]. The present work is focused on the plane-symmetric orbit.

C.   Bifurcations into Resonant Families

Computation of resonant orbits is based on bifurcations from a generating periodic family (e.g., planar 1:1 periodic orbits) [19,21]. The monodromy matrix of a periodic orbit and its eigenvalues and eigenvectors can indicate the resonant families around it. The monodromy matrix is the state transition matrix (STM) of a periodic orbit after one period. The 6×6 STM is the linear map from an initial state to a later state. For details of computing the STM in the CR3BP, readers are referred to Ref. [22]. In the Hamiltonian CR3BP system, the monodromy matrix has three pairs of eigenvalues. Each pair of eigenvalues has the relationship $\lambda_i \cdot \lambda_j = 1$ [23]. If λ_i and λ_j are complex conjugated eigenvalues, they can be represented by $\lambda_i = \cos(\theta) + i \sin(\theta)$ and $\lambda_j = \cos(\theta) - i \sin(\theta)$ (where i is the imaginary unit), respectively. Let e_i and e_j denote the eigenvectors associated with λ_i and λ_j. An infinitesimal displacement in the span $\{e_i, e_j\}$ will rotate θ per period. To form a closed resonant orbit in the vicinity of the reference orbit, the accumulated phase difference should be $2k\pi$, where k is a positive integer. The number of revolutions of the reference motion for the resonant orbit is

$$n = \frac{2k\pi}{\arccos(\lambda_i + 1/\lambda_i/2)} \qquad (5)$$

where n is also a positive integer. If $\{e_i, e_j\}$ is constrained in the plane, a family of horizontal resonant orbits of multiplicity n intersects with the generating family. Similarly, if $\{e_i, e_j\}$ forms a span in the third dimension (i.e., having z and $\dot{z}$ components), the vertical family of multiplicity n intersects with the generating family.

For the problem of interest, the generating family, planar 1:1 QSO (referred to as the 2D QSO hereafter) is first computed. Finding 3D QSOs is based on the vertical n/k of 2D QSOs. For a given n/k, fitting integers for n and k can be chosen. The corresponding 3D QSO has a resonance of $(n - k):n$, where $n - k$ indicates the number of vertical revolutions.

D.   Differential Correction

References [22,24] have given steps of differential correction to compute periodic solutions in the CR3BP, taking advantage of the symmetry. The initial guess of the 3D solution in the vicinity of the reference 2D QSO can be set to the 2D solution. Recall that there are at least two perpendicular crossings of the x-z plane for the plane-symmetric periodic orbits. Let $(x_0, 0, z_0, 0, \dot{y}_0, 0)^T$ denote the initial condition of the 3D QSO, where $y_0 = 0$, $\dot{x}_0 = 0$, and $\dot{z}_0 = 0$ indicate that the initial condition crosses the x-z plane perpendicularly; z_0 represents the z amplitude, which is fixed to a small value for the first near-planar 3D QSO to be recovered; and the initial guess for the set $(x_0, \dot{y}_0)$ of the first 3D QSO can be properly set to $(x_0^{2D}, \dot{y}_0^{2D})$, which represents the initial condition of the 2D QSO on the x axis.

The periodic orbit should perpendicularly cross the x-z plane once again at half a period, $T/2$, or the mth crossing of the x-z plane, where $m = n/2$ for an even n or $m = (n + 1)/2$ for an odd n. $(x_0, \dot{y}_0)$ of the near-planar 3D QSO should be tuned such that $(\dot{x}_{T/2}, \dot{z}_{T/2}) = (0, 0)$ at $T/2$. Integration of the orbit is terminated at the mth plane crossing. In this way, T is naturally updated. Let $\mathbf{\Phi}$ denote the STM, which maps the initial state to the state at the given epoch, and ϕ_{ij} denote the element in the ith row and the jth column of $\mathbf{\Phi}$. The first-order relationship between the free variables and the boundary values at mth crossing is expressed as

$$\begin{bmatrix} \delta \dot{x}_{T/2} \\ \delta \dot{z}_{T/2} \end{bmatrix} = \begin{bmatrix} \varphi_{41} - \dfrac{\ddot{x}\varphi_{21}}{\dot{y}} & \varphi_{45} - \dfrac{\ddot{x}\varphi_{25}}{\dot{y}} \\ \varphi_{61} - \dfrac{\ddot{z}\varphi_{21}}{\dot{y}} & \varphi_{65} - \dfrac{\ddot{z}\varphi_{25}}{\dot{y}} \end{bmatrix}_{T/2} \begin{bmatrix} \delta x_0 \\ \delta \dot{y}_0 \end{bmatrix} \quad (6)$$

Based on this relationship, an iterative differential correction is performed to reduce $\dot{x}_{T/2}$ and $\dot{z}_{T/2}$ to a defined small value. The initial condition, as well as the period of the desired resonant 3D QSO, is then obtained.

E. Continuation of a Resonance Family

Once the solution of the resonant QSO with small z amplitude A_z (i.e., $= z_0 \times LU$) has been computed as explained in the previous section, the 3D family consisting of this orbit can be recovered using the pseudo-arclength continuation method [25]. High-A_z orbits are expected to obtain in this way. z_0 is added to the set of free variables. Equation (6) is extended into

$$\begin{bmatrix} \delta \dot{x}_{T/2} \\ \delta \dot{z}_{T/2} \end{bmatrix} = \begin{bmatrix} \varphi_{41} - \dfrac{\ddot{x}\varphi_{21}}{\dot{y}} & \varphi_{43} - \dfrac{\ddot{x}\varphi_{23}}{\dot{y}} & \varphi_{45} - \dfrac{\ddot{x}\varphi_{25}}{\dot{y}} \\ \varphi_{61} - \dfrac{\ddot{z}\varphi_{21}}{\dot{y}} & \varphi_{63} - \dfrac{\ddot{z}\varphi_{23}}{\dot{y}} & \varphi_{65} - \dfrac{\ddot{z}\varphi_{25}}{\dot{y}} \end{bmatrix}_{T/2} \begin{bmatrix} \delta x_0 \\ \delta z_0 \\ \delta \dot{y}_0 \end{bmatrix} \quad (7)$$

Let B represent the matrix on the right-hand side of Eq. (7). As the neighborhood solution should keep $(\dot{x}_{T/2}, \dot{z}_{T/2}) = (0, 0)$, the direction of the continuation curve is along the null space of B. Let $\bar{i}_s$ denote the unit vector of this direction. The jth element of i_s is expressed as

$$\bar{i}_{sj} = \pm B_j / \sqrt{\sum_{i=1}^{3} B_i^2} \quad (8)$$

where B_j is the determinant of the matrix obtained from B by deleting the jth column times $(-1)^j$. $\bar{i}_s$ is obtained from the last iteration of solution correction. Let u represent the solution vector $[x_0, z_0, \dot{y}_0]^T$, $\tilde{u}$ represent the initial guess of u, and superscript i indicate the ith solution. Given a small size of the pseudo-arclength, S, $\tilde{u}^i$ is computed from

$$\tilde{u}^i = u^{i-1} + \bar{i}_s^{i-1} \cdot S \quad (9)$$

The solution u^i should be tuned around the guess $\tilde{u}^i$. However, as z_0 has been added to the set of free variables, Eq. (7) becomes underdetermined. To amend this, a constraint of the pseudo-arclength is introduced. Equation (7) is modified into

$$\begin{bmatrix} \delta \dot{x}_{T/2} \\ \delta \dot{z}_{T/2} \\ \delta S \end{bmatrix} = \begin{bmatrix} \varphi_{41} - \dfrac{\ddot{x}\varphi_{21}}{\dot{y}} & \varphi_{43} - \dfrac{\ddot{x}\varphi_{23}}{\dot{y}} & \varphi_{45} - \dfrac{\ddot{x}\varphi_{25}}{\dot{y}} \\ \varphi_{61} - \dfrac{\ddot{z}\varphi_{21}}{\dot{y}} & \varphi_{63} - \dfrac{\ddot{z}\varphi_{23}}{\dot{y}} & \varphi_{65} - \dfrac{\ddot{z}\varphi_{25}}{\dot{y}} \\ \bar{i}_{s1} & \bar{i}_{s2} & \bar{i}_{s3} \end{bmatrix}_{T/2} \begin{bmatrix} \delta x_0 \\ \delta z_0 \\ \delta \dot{y}_0 \end{bmatrix} \quad (10)$$

Based on this relationship, the differential corrector can find the next solution, which is a pseudo-arclength of S away. For more details of correction and continuation, see Ref. [26].

F. Linear Stability

As the monodromy matrix M is essentially a linear mapping, the linear stability of an orbit is described by the maximum modulus of eigenvalues of M, $\|\lambda\|_{\max}$. On the other hand, for situations with $\|\lambda\|_{\max} > 1$, this quantity increases exponentially with the number of revolutions. Given that different resonant families experience different numbers of revolutions, the stability index should be normalized

for a fair comparison between families. The normalized stability index ν used in this work is expressed as

$$\nu = \sqrt[n]{\|\lambda\|_{\max}} \quad (11)$$

If $\nu = 1$, the periodic orbit is linearly stable. If $\nu > 1$, the orbit is unstable.

G. Full Dynamic Model

The full dynamic model is used to produce realistic trajectories and verify results obtained in lower-fidelity models. The full dynamic model used in this work takes into account the ephemerides of the Sun, Mars, and Phobos; the gravity field of Mars up to degree and order 10; and the gravity field of Phobos up to degree and order 4. The ephemerides and orientation of Mars and Phobos bodies are obtained through the Jet Propulsion Laboratory (JPL) SPICE routine. The solar radiation pressure is not included in this work, because of its insignificant effect and the lack of information on the spacecraft.

III. Families of 3D QSO and Their Linear Stability

2D QSOs are first computed for deriving resonant 3D QSOs. The initial conditions and periods as a function of the x amplitude (i.e., $A_x = (x_0 - 1 + \mu) \times LU$) of 2D QSOs are shown in Fig. 2. The period ranges from 4 to 7 h for 2D QSOs with A_x from 20 to 60 km. Figure 3 shows the family of 2D QSOs in the Phobos-centered rotating frame. The horizontal and vertical n/k of the 2D-QSO family are computed from Eq. (5), which are also shown in Fig. 3. Finding 3D QSOs is based on vertical n/k. As the minimum vertical n/k is 4.3, the multiplicity of a 3D QSO is at least 5.

A. Solution Map and Influence of Horizontal Bifurcations

Families of resonant 3D QSOs are computed using differential correction and pseudo-arclength continuation (see Secs. II.D and II.E). However, it is common that the process of continuation encounters a singularity where a pair of unity eigenvalues of the monodromy matrix emerges. For the problem of interest, at the singularity point, $\text{rank}(B) < 2$ and $\sqrt{\sum_{i=1}^{3} B_i^2} = 0$ [see Eq. (8)]. In that case, if the limit of Eq. (8) as $\sqrt{\sum_{i=1}^{3} B_i^2}$ approaches zero along the continuation curve exists, there is still a solution for $\bar{i}_s$ [26,27]. However, at that point, $\bar{i}_s$ usually exhibits a turn, giving rise to a secondary branch. Observations of solution curves for the problem of interest show that solutions of secondary branches do not extend to higher-A_z regions as desired.

Recalling the Lyapunov-halo bifurcation, the 3D halo orbit bifurcates from the planar Lyapunov orbit for a similar cause. However, in that situation, because there are two solution directions in the spatial and planar space, the continuation of planar Lyapunov solutions is not interrupted by the bifurcation to the halo family. As for the problem of
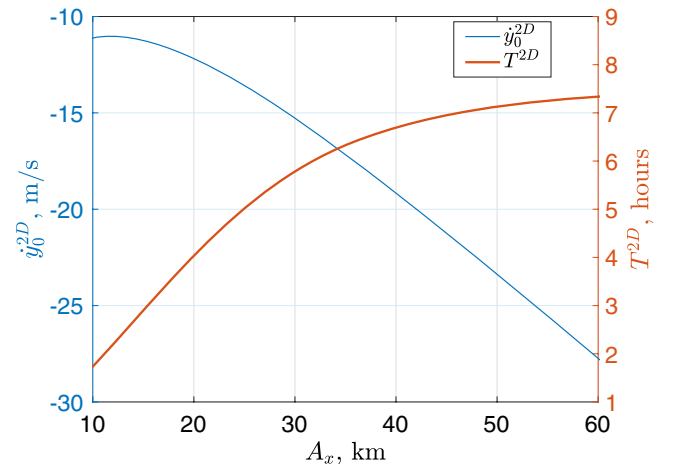

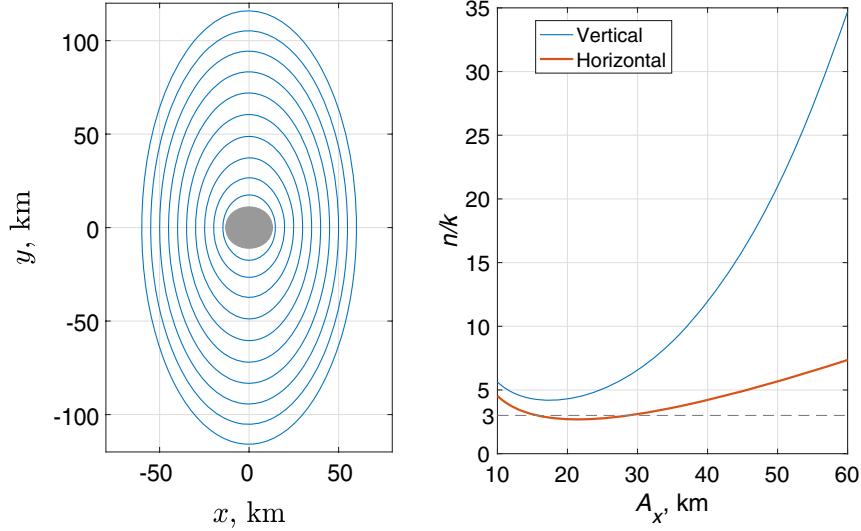**Fig. 2   Initial condition and periods of 2D QSO family.**

Fig. 3   Two-dimensional QSOs (left) and vertical and horizontal n/k (right).

interest, there are three nontrivial elements in the solution, and thus only one solution direction exists in the spatial space. Nevertheless, it can be speculated that the solution curve of the primary branch recovers on the other side of the singularity point. With this hypothesis, before reaching the vicinity of the singularity point, $\bar{i}_s$ is computed and a large S is applied to obtain an initial guess [see Eq. (9)] along the presumed extended primary branch on the other side of the singularity. Starting from that initial guess, the differential corrector succeeded in reaching the solution belonging to the primary branch on the other side.

The solution map of families of periodic 3D QSOs computed as explained above is shown in Fig. 4. Note that, for conciseness, not all resonance ratios are annotated. In addition, for simplicity $\dot{y}_0$ is not

Fig. 4   Solution and linear-stability map of 3D QSO families found in the CR3BP.

displayed in the figure, and therefore the intersection of solutions projected on the A_x-A_z map does not suggest the same orbit. The figure shows that continuation of many primary branches is interrupted by the turns into secondary branches in the low-A_z region. With the "singularity-skipping trick" described above, solutions with high A_z have been recovered.

Figure 5 shows examples of orbits with $A_x = 30$ km from primary branches. The size of the orbit is represented in the $A_x \times A_y \times A_z$ format, where the y-amplitude A_y is the maximum value on the $+y$ axis. Figure 6 shows orbits with $A_x = 30$ km from secondary branches. By comparison, orbits from primary branches are neater, and orbits from secondary branches exhibit greater horizontal variations. The reason is that the secondary branch is a result of the intersection of vertical and horizontal bifurcations. That is also why secondary branches do not extend to the high-A_z region. These orbits with large horizontal variations are referred to as the "swing QSO," and identified as possible transfer orbits between QSO in other works (e.g., Refs. [16,28]).
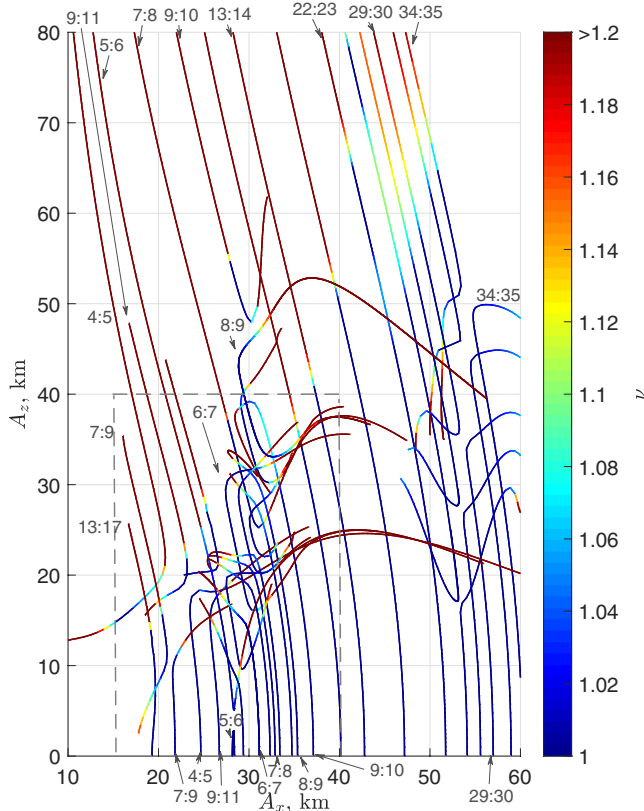
B.   Linear-Stability Region

The linear-stability index of each 3D QSO is computed as given in Sec. II.F. The linear stability of each orbit is indicated by the color scale (see the digital version) in Fig. 4. The solution space around states of periodic QSOs is filled by states of quasi-periodic QSO, which are also bounded motions around Phobos. Through an exploration of periodic families, the linear-stability region of bounded orbits can be revealed. It can be seen in the figure that the highest A_z of stable orbits generally increases with A_x, except for two bulges at $A_x = 28$ km and $A_x = 41$ km, where A_z of stable orbits extends to 54 and 75 km, respectively. The orbits chosen to display in Figs. 5 and 6 are from the linear-stability region.

The broad stability region revealed by the linear stability of many periodic orbits seems to be favorable for mission operations. However, linear stability is only a necessary condition for orbital stability. It does not sufficiently ensure a stability domain for operation. In addition, the CR3BP is a simplified model not considering the effect of the eccentricity of Phobos' orbit and nonspherical gravity fields. For guiding operations, effective stability levels of QSOs are characterized in the following section.

IV.   Sensitivity Analysis

The objective of this section is to evaluate the effective stability of QSOs, in terms of the freedom of injection timing and robustness to operational errors. Note that the effect of modeling errors of nonspherical gravity fields is not discussed in this paper. Current knowledge of the gravity field of Mars is sufficiently accurate. The uncertainty of the terms C_{20} and C_{22} of the gravity field of Phobos is 10% [29,30]. Errors
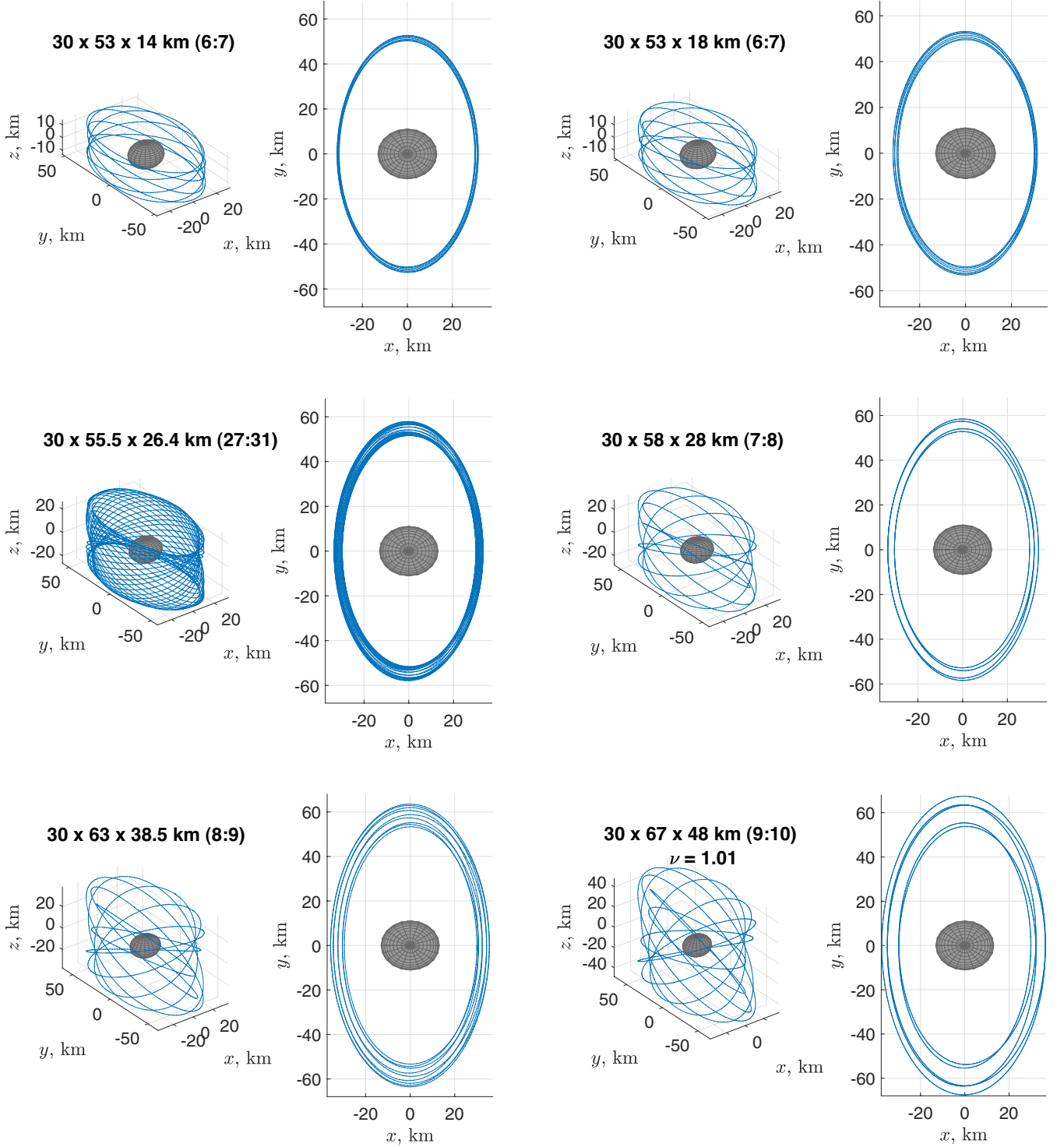
Fig. 5   Stable 3D QSO found in primary branches at $A_x = 30$ km.

of such an order are observed to hardly influence the QSO with $A_x > 20$ km concerned in this work. Regarding the altitude of interest, the motion that comes close to Phobos is the most interesting in terms of applications, while being at the same time tricky when it comes to risk assessment. The following sensitivity analysis is focused on the QSO of low A_x, namely, below 40 km. The block framed by the dashed lines in Fig. 4 represents the QSOs of interest. Concerning the time interval, critical operations such as maneuvers need to be executed with good visibility conditions from the Earth. In addition, a sufficiently long time (i.e., typically 7 days) is needed by the orbit determination to reach acceptable accuracy. For these reasons, orbit maintenance controls cannot be implemented frequently. Therefore, a 7-day interval is used to examine the behavior of perturbed QSOs in this section.

A.   Residual Index

In what follows, the periodic orbit in the simplified model (i.e., CR3BP) is referred to as the nominal orbit. The orbit perturbed in the same CR3BP or a different dynamic model is referred to as the truth orbit. A residual index is defined to describe the deviation of the truth orbit with respect to the nominal orbit. Observations based on numerical simulations show that a divergent orbit generally deviates quickly along the y direction in the rotating frame; and if the orbit reaches a distance <15 km from the center of Phobos, it is about to escape or impact on the target soon.

Regarding the first observation, y coordinates of the truth orbit and the nominal orbit at y-z plane crossings are compared. The residual is then normalized by the y coordinate of the nominal state for a fair
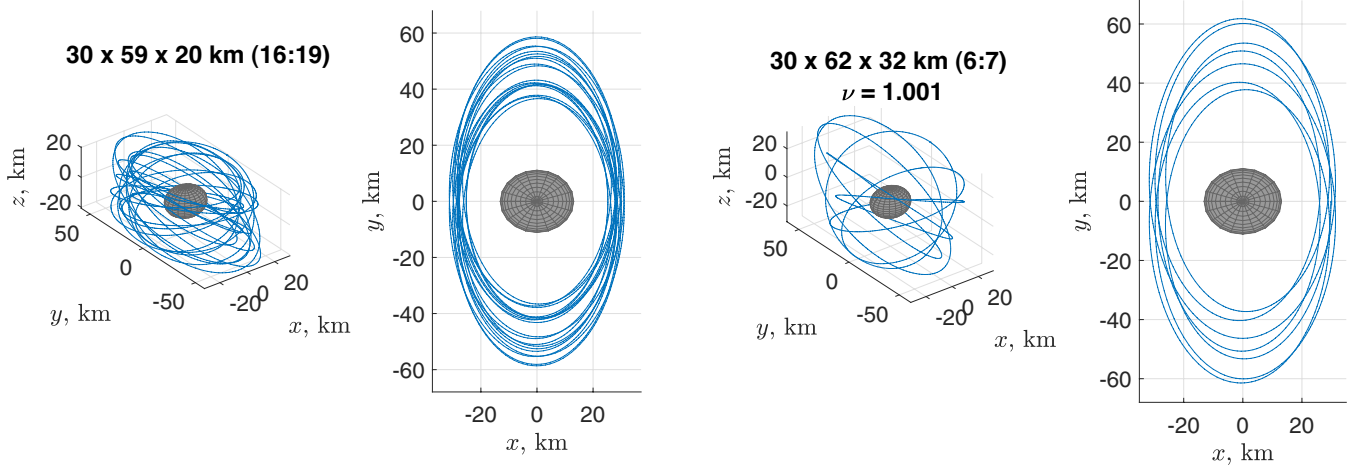
Fig. 6   Stable 3D QSO found in secondary branches at A_x = 30 km.

comparison. The average of the residuals indicates the fluctuation amplitude of the truth orbit with respect to the nominal orbit. Additionally, the final residual is also an important indicator. Regarding the second observation, when the closest approach $r_{min} < 15$ km, the residual is set to infinity to indicate a coming impact or escape. To conclude, the residual index Res is expressed as

$$Res = \begin{cases} 0.5\left(\sum_{i=1}^{N}\left|\dfrac{\bar{y}_i - y_i}{\bar{y}_i}\right|\right)/N + 0.5\left|\dfrac{\bar{y}_N - y_N}{\bar{y}_N}\right| & \text{if } r_{min} \geq 15 \text{ km} \\ \infty & \text{if } r_{min} < 15 \text{ km} \end{cases}$$

(12)

where $\bar{y}_i$ and y_i are the y coordinates of the nominal and truth orbits at the ith y-z plane crossing, respectively, and N is the minimum of the numbers of plane crossings of the two orbits. Note that differences between $\bar{y}_i$ and y_i are obtained at corresponding crossings instead of corresponding times. In this way, the in-track difference or phase drift, which is less critical for operation, is neglected. The average and final residual parts in the first equation are equally weighted by 0.5. It is observed in many numerical simulations that orbits with $Res < 0.2$ are closely bounded around its nominal orbit; orbits with $Res < 0.3$ stay bounded around Phobos; and orbits with $Res \geq 0.3$ are considered no longer bounded, which can diverge during the 7-day interval or quickly afterward. The following sensitivity analyses adopt the defined residual index.

B.   Effect of Eccentricity and Nonspherical Gravity Fields

1.   J2-Elliptic Model

Because of the eccentricity of Phobos' orbit, the epoch of the initial condition of the QSO will influence the orbit behavior. Nevertheless, the initial epoch t_0 can be generalized by the initial true anomaly of Phobos' orbit, f_0. To quickly examine orbit behaviors in various situations without losing much accuracy, a model referred to as the J2-Elliptic model and depending on f_0 is developed. The J2-Elliptic model is set up based on the work of Wiesel [17]. It is assumed in the model that Phobos moves in the Mars J2-perturbed Keplerian orbit, the equatorial planes of Mars and Phobos are aligned, and Phobos is entirely tidally locked with its principal axis always pointing to Mars' center of mass. The coordinate system used in this work is with the origin set at the center of mass of Mars, the X axis fixed in the inertial space and in the direction from Mars to Phobos at t_0, the Z axis normal to orbital plane of Phobos, and the Y axis completing the right-handed coordinate system. The coordinate system of the J2-Elliptic model is schematically depicted in Fig. 7. The position and orientation of Phobos are computed based on the mean elements of the J2-perturbed orbit, which are given in the Appendix.

The orbit of the spacecraft is integrated in this inertial frame. As the orbit of Phobos is influenced by Mars' J_2, the integration of the trajectory
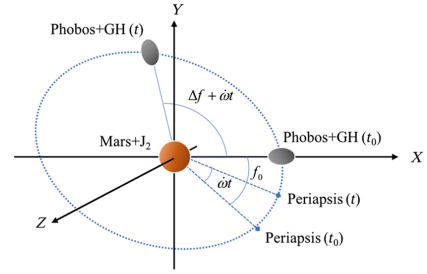

Fig. 7   Schematic of the J2-Elliptic system.

of spacecraft should also take into account this term. In addition, as the nonspherical gravity field of Phobos barely influences its own orbit with respect to Mars but can influence the motion of the spacecraft, it is also included in this dynamic model. As the J2-Elliptic coordinate depends on the initial phase of Phobos along its orbit, or f_0, all initial configurations can be easily covered by varying f_0 from 0 to 360°.

Note that higher-degree terms of Mars' gravity field, inclination of Phobos' orbit (1.08°) and the libration amplitude of Phobos (1.1°), are neglected in the model. The perturbation induced from the small libration on the QSO with $A_x > 20$ km is negligible. To justify the neglect and examine the fidelity of the J2-Elliptic model, the model is compared with the full dynamic model (see Sec. II.G) by examining profiles of propagated orbits and the Res (i.e., Eq. (12)) with respect to the nominal orbit. Res obtained in the J2-Elliptic model and the full dynamic model are denoted by Res_{JE} and Res_{FD}, respectively. Figure 8 shows four of the comparison cases and indicates the corresponding Res_{JE} and Res_{FD}. It can be seen that the orbits in the J2-Elliptic model closely follow that in the full dynamics in various cases with small, medium, large, and escaping residuals.

2.   Investigation in the J2-Elliptic Model

Initial conditions of periodic QSOs obtained in the CR3BP are converted to the J2-Elliptic model for given f_0 and propagated for 7 days. Note that no adjustment is applied to the converted initial condition, as the objective of this analysis is to find which initial conditions can always lead to bounded motions regardless of the initial epoch. By varying f_0 from 0 to 360°, Res are obtained as a function of f_0 for each orbit. In this work, the sampled f_0 are evenly spaced by 1°. The ratio of the f_0 leading to $Res < 0.3$ for a 3D QSO is regarded as the ratio of bounded motions. The left panel of Fig. 9 presents the ratio of bounded motions under varied f_0 for each orbit through the color scale.

C.   Effect of Operational Errors

Operational errors include navigation and Δv execution errors. To examine the orbital sensitivity to operational errors, the initial
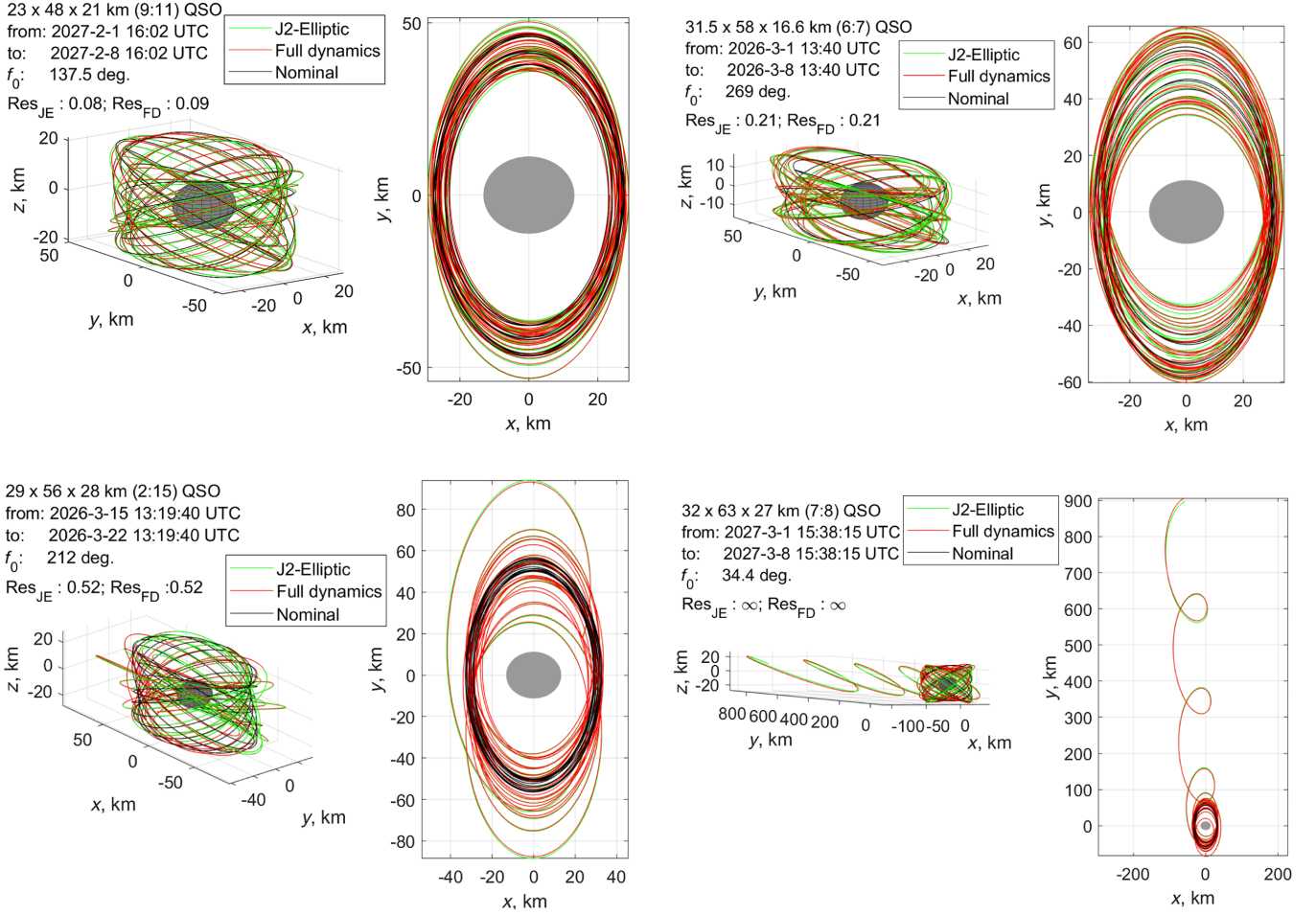
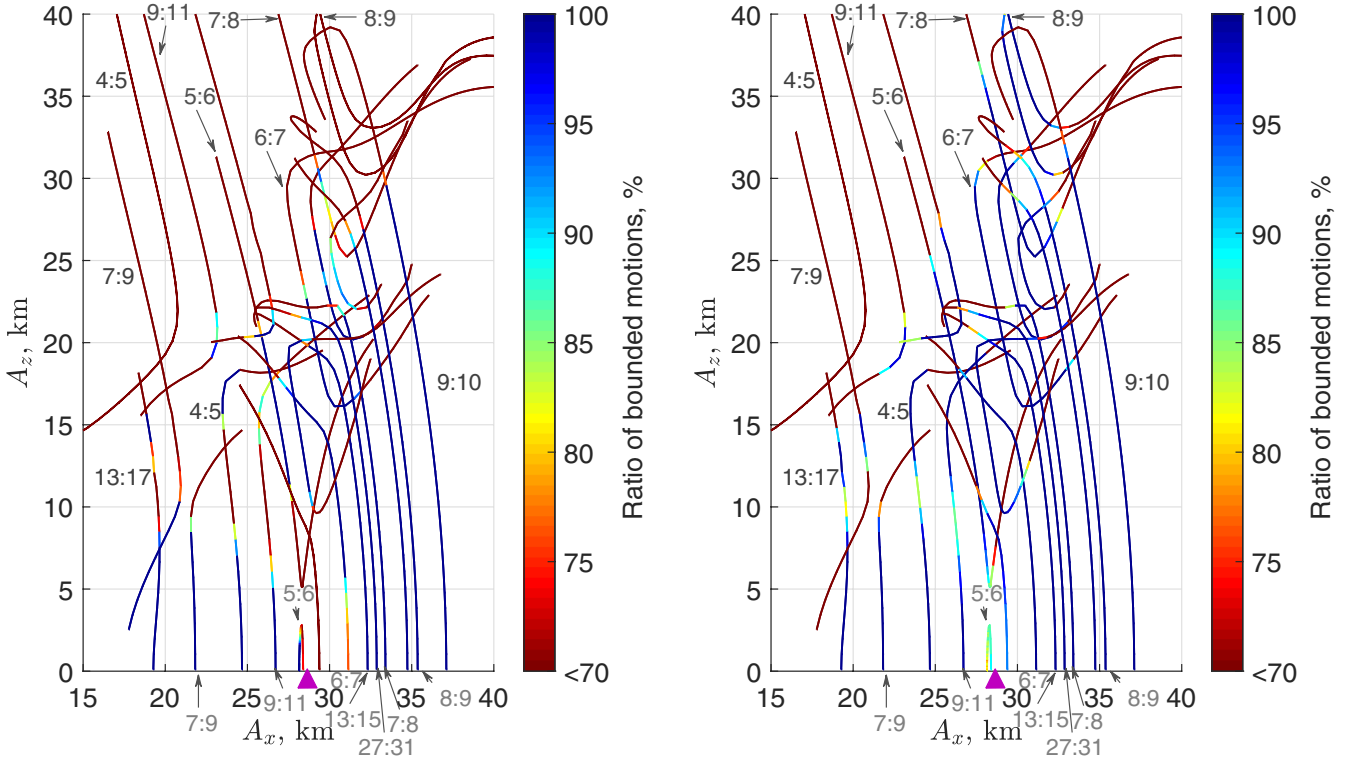**Fig. 8 Examples of comparing the J2-Elliptic model to the full dynamic model.**

Fig. 9 Sensitivity of 3D QSO to the initial phase (left) and to operational errors (right).

Navigation position, m	Navigation velocity, m/s	Δv norm, %	Δv direction, deg
150	0.09	5	0.1

condition of the periodic 3D QSO is perturbed by these errors, and propagated in the CR3BP for 7 days. The assumed values for the navigation and Δv execution uncertainties are summarized in Table 1. The execution error depends on the magnitude of correction Δv. A Δv root-sum-square (RSS) uncertainty of 2.4 cm/s (i.e., 1σ 1.4 cm/s on each component) is used in the sensitivity analysis. The preliminary result of orbit maintenance (i.e., ΔvRSS uncertainty is up to 1.6 cm/s) presented in Sec. V.A shows that the assumed quantity is reasonable and conservative. For each orbit, 1000 Monte Carlo runs are performed with errors randomly generated according to the given uncertainties. The ratio of cases with $Res < 0.3$ (i.e., ratio of bounded motions) for each orbit is obtained. The right panel of Fig. 9 shows the ratio of bounded motions under random operational errors.

By comparing the two plots in Fig. 9, it can be seen that the eccentricity of Phobos' orbit is more influential than the operational error in perturbing the QSOs. An exception to this statement is the secondary branch of the upper 7:9 family, where the operational error is more influential.

D. Instability Caused by Unstable Resonance

The comparison of Fig. 9 and Fig. 4 exhibits an instability region inside the linear-stability region expanding from $A_x = 28$ km on the plane (labeled by the triangle marker) to higher A_z and smaller A_x. The planar instability region around $A_x = 28$ km is consistent with results of Ikeda et al. [16] and Wiesel [17], who examined QSO sensitivity to injection errors in the planar problem. Hénon [31], Benest [10], and Lam and Whiffen [32] have noted that the stability domain of a planar QSO is confined by the planar period-3 orbit (i.e., the planar resonant family that bifurcates at horizontal $n/k = 3$). In other words, at the intersection of QSO family with the period-3 orbit family, the stability domain of the QSO decreases to zero, despite the linear stability the QSO presents. Previous work [33] using Poincaré maps to study stability domain of QSOs around Phobos reveals this phenomenon. The horizontal n/k shown in Fig. 3 indicates that the intersection with period-3 orbit occurs at $A_x = 15.5$ km and $A_x = 28.5$ km. Whereas Fig. 4 implies that low-inclination QSOs are generally more stable than high-inclination QSOs, the sensitivity analysis shows a contrasting phenomenon for QSOs with A_x near 30 km, where high-inclination QSO can be more stable. It is not recommended to send the spacecraft to a planar QSO with A_x between 27 and 30 km in early phases of the mission. For that A_x interval, 3D QSO with certain inclinations can serve as more robust replacements.

E. Effective Stability Levels

Results of the sensitivity analyses in previous subsections can be exploited for mission design purposes. For instance, the orbit with $Res < 0.2$ stays bounded around its nominal orbit and thus can be easily maintained by a correction maneuver. While the orbit with $0.2 < Res < 0.3$ is bounded around the target, it may not be easily pulled back to its nominal orbit by a single impulse after 7 days. To serve the goal of selecting QSO for both long-term and temporary orbiting, effective stability levels are defined according to Res obtained from the sensitivity analyses. Let p_1^ρ represent the ratio of cases satisfying $Res < \rho$ under varied f_0, and p_2^ρ the ratio of cases satisfying $Res < \rho$ under random operational errors. The product $P_\rho = p_1^\rho \times p_2^\rho$ suggests the theoretical probability that Res of the truth orbit in the realistic dynamic environment is smaller than ρ. A classification based on this statistical implications is suggested as follows:

1) Hyperstable level: $P_{0.2} > 99\%$. It suggests that the truth orbit can be maintained by control Δv at intervals of 7 days with <1% risk

of failure. Hence, the orbit is a candidate for long-term orbiting that can be implemented by most missions.

2) Superstable level: $P_{0.3} > 99\%$. It suggests that temporary orbiting can be performed with <1% risk of collision or escape, which is acceptable for most missions.

3) Stable level: $90\% < P_{0.3} \leq 99\%$. It suggests that the failure rate of temporary-orbiting operations is between 1 and 10%, which is acceptable for low-cost missions, such as nanospacecraft missions.

4) Weakly stable level: $75\% < P_{0.3} \leq 90\%$. It suggests that the failure rate of temporary-orbiting operations is between 10 and 25%. Orbits of this level may be adopted by missions recovered from severe problems and not possessing much flexibility.

5) Unstable level: the rest of the QSO solutions. These orbits have a probability of successful orbiting around Phobos < 75%. It is recommended to avoid these orbits, unless, for instance, supplementary navigation operation methods are established to enable sophisticated orbit control. The classification of QSOs according to the defined effective stability levels is depicted by the color scales in Fig. 10.

V.   Explorations in the Full Dynamic Model

To verify the effective stability levels concluded in the mid- and low-fidelity models and to demonstrate the practical application, investigations in the full dynamic model (see Sec. II.G) are conducted in this section. In particular, orbit maintenance trials are demonstrated, and massive Monte Carlo runs for a long time span (i.e., 21 days) are performed to examine the relation of those results with the long-term stability of QSOs. In view of the results of this section, one can determine up to which extent the effective stability levels reflect the orbit behaviors in reality.

A. Orbit Maintenance

It can be inferred from the sensitivity analysis that orbit maintenance of a low-altitude QSO is challenging. As the stability region is confined by the period-3 family, a small perturbation can hence shift the orbit into the instability region. Moreover, the orbit determination campaign takes approximately 7 days to reach the baseline accuracy listed in Table 1. Nevertheless, sensitivity analyses have also revealed hyperstable orbits that can naturally stay around the nominal orbit for at least 1 week. These orbits are considered maintainable with sparsely placed Δv and are used in this analysis.
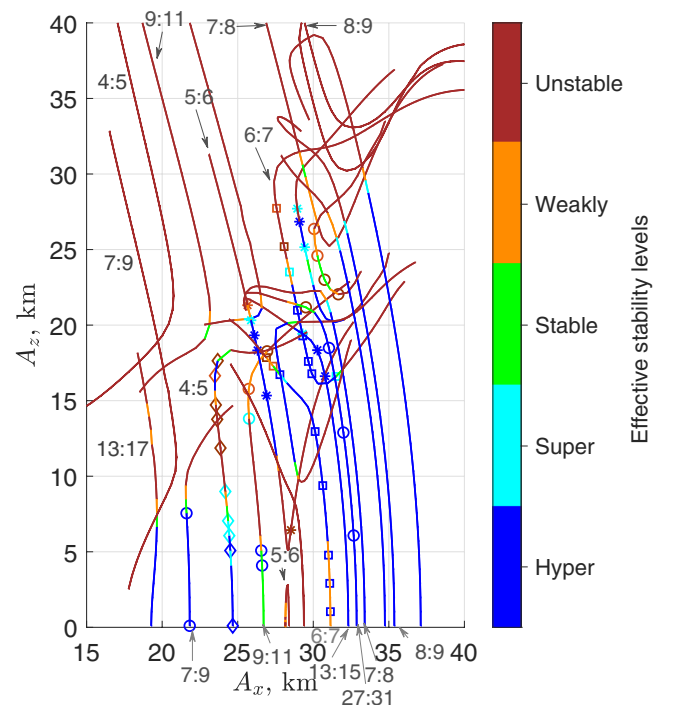

Fig. 10   Effective stability levels (color scales) and results (markers) of 21-day dispersion simulations.

Table 2 Parameters of nominal 3D QSOs and results of station keeping

Item	Trial 1	Trial 2	Trial 3
Nominal amplitude, km	22×31	$29 \times 53 \times 21$	$29.7 \times 53 \times 17.6$
Average control interval, day	7.2	8.4	8.6
Average control Δv, cm/s	37.5	93.7	93.4
ΔvRSS uncertainty, cm/s	0.6	1.5	1.6

Table 2 gives information of three examined hyperstable orbits: 22 km × 31 km (2D QSO), 29 km × 53 km × 21 km, and 29.7 km × 53 km × 17.6 km (both 3D QSO belonging to the 6:7 family). The initial condition of a nominal orbit is used to generate baseline orbits in the full dynamic model. The correction Δv is placed at a point after 7 days when the propagated state is close to the nominal initial condition converted in the full dynamic model at the corresponding epoch. Each Δv is applied in order to make the following leg be as close as possible to the corresponding baseline leg. To be specific, a three-component $\Delta \boldsymbol{v}$ is resolved to minimize differences between the corrected leg and the baseline leg at a series of epochs, in a least-square sense. To compute $\Delta \boldsymbol{v}$ quickly and robustly, the STM is integrated along with the orbit. The gradient of differences with respect to $\Delta \boldsymbol{v}$ can be derived from the STM. $\Delta \boldsymbol{v}$ is adjusted using the gradient-based differential correction method. The simulated orbit maintenance operation for this study starts at 2026-02-01 16:00 UTC and continues for 30 legs (i.e., longer than 7 months). Note that both navigation errors and Δv execution errors (see Table 1) are considered in the simulation.

Table 2 lists results of three orbit maintenance trials for the selected nominal QSOs. The Δv cost is around 40 cm/s per week for the maintenance of the planar orbit, and around 1 m/s per 9 days for that of the 3D orbits, which is considered acceptable for many missions. Figure 11 shows the maintained orbit legs for the 29 km × 53 km × 21 km QSO. The robustness of the orbit maintenance confirms the effective stability of the candidate orbits under realistic dynamics. In a realistic mission scenario, the spacecraft can always park on these candidate orbits before and after a certain proximity operation.

For the maintenance trial of 29 km × 53 km × 21 km QSO, the maximum inclination of maintained legs ranges from 38 to 45°. Figure 12 presents the ground track of one leg. As is shown, the maximum inclination is 40°, and the ground track intensively covers the interesting Stickney crater (i.e., latitude between −20 and −22° and longitude between −70 and −28°) [34]. The distance to the surface of Phobos ranges from 19 to 47 km. These characteristics, along with an affordable long-term maintenance cost, can greatly benefit the science return of the mission.

B. Long-Term Stability

Sensitivity analyses in Sec. IV are performed in simplified and midfidelity models with propagation intervals limited to 7 days. It is interesting to verify long-term behaviors of QSOs in full dynamics
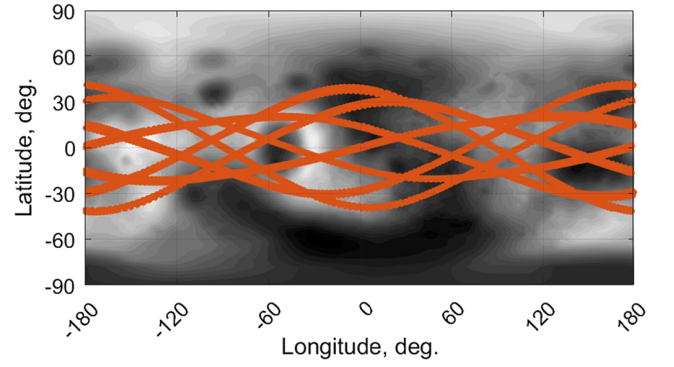
Fig. 12 The ground track of a maintained leg for the 29 km × 53 km × 21 km QSO.

and confirm up to which extent they correspond to the effective stability levels implied by the sensitivity analyses.

1. Monte Carlo Simulations

For this purpose, Monte Carlo simulations are performed in full dynamics with a time span of 21 days, which is a tradeoff between the observation of the long-term trends and computational time. Furthermore, different from what has been presented previously in this paper, a least-squares fitting of the truth trajectory (i.e., in the full dynamics) to the nominal orbit (i.e., computed in CR3BP) over a time span of 2 days, has been applied to the initial conditions. Finally, note that the sensitivity analysis of the initial phase of Phobos f_0 has revealed bad case values (i.e., the f_0 resulting in maximum Res) for some orbits. The corresponding worst-case dates have been chosen for the Monte Carlo simulations in order to analyze the most conservative scenario.

Batches of 50×10^3 random draws of the navigation errors in Table 1 have been used to perturb the adjusted initial states of selected 3D QSOs. During the 21-day interval, if the dispersed trajectory reaches a radius of 15 km with respect to the center of mass of Phobos, it is considered to be a colliding trajectory and not integrated further. In the same way, when the distance of propagated state from Phobos exceeds 500 km, the trajectory is considered as an escape trajectory. At the end of each simulation, statistics of bounded motion (i.e., excluding the collision and escape cases) corresponding to a given initial condition are obtained.

2. Results

For the sake of briefness, only representative results of the Monte Carlo simulations have been chosen and listed in Table 3. Columns 2–4 show the information of the nominal periodic QSO. Columns 5–7 present results from the sensitivity analyses in Sec. IV as a reference. Here, the stability levels from hyperstable to unstable levels are indexed from 1 to 5 (see Sec. IV.E for the correspondence). The f_0 column indicates the bad f_0 where the simulations start. The results
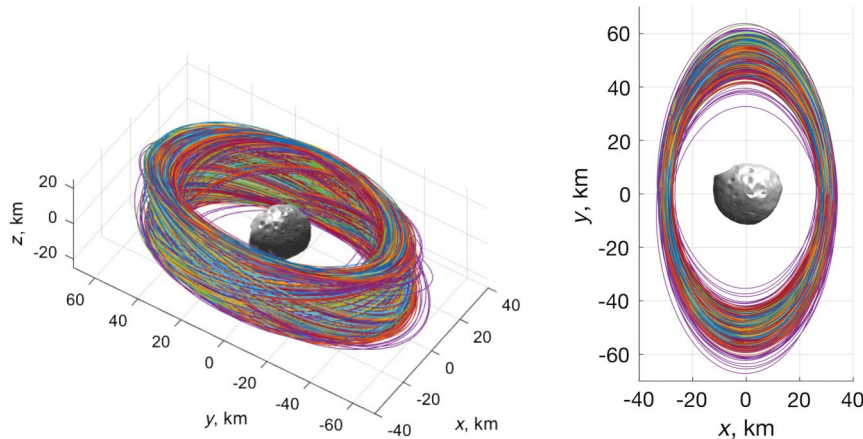

Fig. 11 The maintained 29 km × 53 km × 21 km QSO from 2026-02-01 12:00 to 2026-10-10 14:19 UTC.

Table 3 Sample of the results of the 21-day dispersion analyses

No.	Amplitude, km	Resonance ratio	Period, days	% Res < 0.2 for all f_0	% Res < 0.2 under operational errors	Stability level	f_0, deg	% Bounded motion
1	$21.8 \times 30.7 \times 0.1$	7:9	1.66	100	100	1	0	100
2	$24.7 \times 36.8 \times 0.1$	4:5	1.03	100	100	1	0	99.1
3	$32.7 \times 55.7 \times 6$	27:31	7.91	100	100	1	206	100
4	$30.6 \times 51 \times 9.4$	6:7	1.74	100	100	1	315	100
5	$30.1 \times 51 \times 12.9$	6:7	1.74	100	100	1	0	100
6	$26.9 \times 46.5 \times 15.3$	5:6	1.42	100	100	1	189	99.9
7	$23.5 \times 42.5 \times 16.6$	4:5	1.09	100	100	1	218	79.8
8	$29.7 \times 53 \times 17.6$	6:7	1.76	100	100	1	206	100
9	$31 \times 56.8 \times 18.5$	27:31	8.00	100	100	1	0	100
10	$26 \times 46.5 \times 19.3$	5:6	1.43	100	100	1	189	99.7
11	$25.9 \times 46.5 \times 20.3$	5:6	1.44	100	100	1	74	94.5
12	$29 \times 53 \times 21$	6:7	1.76	100	100	1	86	99.9
13	$32.9 \times 56 \times 26.8$	13:15	3.89	100	100	1	258	99.4
14	$29.4 \times 56.1 \times 25.1$	2:15	3.88	100	100	2	149	91.7
15	$21.6 \times 32.7 \times 7.5$	7:9	1.72	100	97.4	3	0	100
16	$30.7 \times 57.7 \times 23$	27:31	8.05	93.6	100	3	0	36.5
17	$30.3 \times 57.4 \times 24.6$	27:31	8.06	93.6	100	3	160	77.2
18	$26.5 \times 41.7 \times 5$	9:11	2.44	90.0	91.8	4	46	99.0
19	$25.7 \times 41.3 \times 15.8$	9:11	2.51	87.5	100	4	63	91.3
20	$25.7 \times 41.3 \times 15.8$	9:11	2.51	87.5	100	4	195	84.5
21	$23.5 \times 40.5 \times 14.7$	4:5	1.08	83.6	100	4	241	26.5
22	$25.6 \times 46.5 \times 21.3$	5:6	1.44	79.2	99.7	4	74	83.7
23	$24.2 \times 38 \times 9$	4:5	1.06	70.1	84.5	5	178	94.3
24	$31.6 \times 61 \times 22$	27:31	8.03	72.8	98.9	5	269	22.5
25	$28 \times 53.4 \times 25.2$	6:7	1.78	62.5	100	5	229	52.1

show that the agreement between the guess provided by the effective levels and the actual percentage of bounded cases in full dynamics for a long time span is remarkable, especially for the so-called hyperstable (or level 1) trajectories. For a graphical representation of the comparison, markers for the particular initial conditions examined via Monte Carlo simulations are added to Fig. 10. The dark blue markers indicate that >99% of the perturbed trajectories survived the 21-day integration (i.e., without reaching the escape or the collision condition) in the full dynamics. The cyan markers indicate >90%, the orange between 75 and 90%, and the red <75%. It can be seen that all the hyperstable initial conditions lead to 90% bounded cases (labeled by blue or cyan marks), and most of them lead to 99% or higher, except for the one near the turning point of the lower 4:5 branch (i.e., sample No. 7 listed in Table 3). Although being classified as hyperstable, this state lies on the boundary between the stability and instability regions. States like this are more likely to become divergent after a long period than those well inside the stability region. Another visible disagreement between the effective stability and realistic behavior appears on the lower segment of the lower 6:7 branch. The sensitivity result in Sec. IV.B indicates an instability in this segment due to the eccentricity of Phobos' orbit. However, simulations in the present section suggest that the adjustment of the initial condition can, up to some extent, cope with the perturbation due to the eccentricity.

A variety of long-term stable motions in the solution space of 3D QSOs are revealed, which are believed to represent a step forward toward the use of these trajectories for Phobos observation. Some promising QSO trajectories with A_x around 30 km and reaching high inclinations are as follows: the lower branch of the 6:7, 13:15, and 27:31 families, with A_z up to 18 km; the upper branch of the 5:6 family with A_z from 12 to 20 km; and the upper branch of the 6:7 family with A_z from 16 to 21 km.

VI. Conclusions

This paper has analyzed the stability of QSOs around Phobos in the spatial problem, with the objective of providing a guideline for the trajectory and operation design of Phobos missions. Families of

resonant 3D QSOs have been computed in the CR3BP. To be specific, continuation and singularity skipping techniques have led to recoveries of high-inclination QSO families. The obtained families of periodic orbits allow for a comprehensive assessment of the stability region. The linear stability concluded in the CR3BP, however, cannot sufficiently indicate a stability domain for operations. Therefore, orbital sensitivity to the initial epoch and operational errors has been analyzed. In particular, the orbital robustness to the initial epoch is revealed via an examination in the J2-Elliptic model, which is a close approximation to the full dynamic model. Effective stability levels (i.e., hyperstable, superstable, stable, weakly stable, and unstable) have been defined according to results of these analyses, revealing the practical stability region, which is confined by the intersection with the period-3 family. As one result of this, at the x amplitude around 28 km, 3D QSOs with certain inclinations enjoy greater stability than low-inclination and planar QSOs. For operations performed near this x amplitude, employing 3D QSO means not only to enhance global mapping, but also to secure operations.

Moreover, orbit maintenance trials in realistic dynamics employing low-altitude 2D and 3D QSO orbits inside the hyperstability region as the baseline orbits have been proven successful. The control frequency and Δv cost (around 1 m/s per 9 days) are considered acceptable for real operations. In addition, long-term stability of hyperstable orbits has also been verified in realistic dynamics by means of massive Monte Carlo simulations. These results have confirmed the practical applicability of the effective stability levels revealed in this work.

Appendix: Elements of the J2-Elliptic Model

The mean semimajor axis $\bar{a}$ and mean motion $\bar{n}$ of the J2-perturbed orbit of Phobos are computed from (for details, see [35])

$$\bar{a} = a\left(1 - \frac{3\bar{R}_{\mathrm{mar}}^2 J_2 \sqrt{1 - e^2}}{2p^2}\right) \tag{A1}$$

$$\bar{n} = n\left(1 + \frac{3\bar{R}_{\mathrm{mar}}^2 J_2 \sqrt{1 - e^2}}{2p^2}\right) \qquad (A2)$$

The osculating semimajor axis $a = 9378$ km, eccentricity $e = 0.0151$, and Mars reference radius $\bar{R}_{\mathrm{mar}} = 3396$ km and $J_2 = 0.00195661$ are used in this work. $\bar{a} = 9374.4$ km is resolved. The mean anomaly, M, true anomaly, f, and the orbital radius of Phobos, R_{mp}, are computed from

$$M_0 = \mathrm{True2Mean}(f_0, e), \qquad M = \bar{n}t + M_0 \qquad (A3)$$

$$f = \mathrm{Mean2True}(M, e), \qquad R_{\mathrm{mp}} = \frac{\bar{a}(1 - e^2)}{1 + e\cos f} \qquad (A4)$$

where True2Mean() and Mean2True() represent the numerical routines to solve for the mean and true anomalies, respectively. The drift rate of periapsis due to Mars J_2 is computed from

$$\dot{\omega} = \frac{3n\bar{R}_{\mathrm{mar}}^2 J_2}{2p^2} \qquad (A5)$$

Let

$$u = \dot{\omega}t + f - f_0 \qquad (A6)$$

For computing Phobos' gravitational force acting on the spacecraft, the rotation matrix from the inertial frame to Phobos body-fixed frame is expressed as

$$\mathrm{Rot}_{\mathrm{ine-pho}} = \begin{bmatrix} -\cos(u) & -\sin(u) & 0 \\ \sin(u) & -\cos(u) & 0 \\ 0 & 0 & 1 \end{bmatrix} \qquad (A7)$$

Phobos position with respect to Mars is expressed as $\boldsymbol{R}_{\mathrm{mp}} = [R_{\mathrm{mp}}\cos(u), R_{\mathrm{mp}}\sin(u), 0]^{\mathrm{T}}$.

Acknowledgments

References

[1] Hunten, D. M., "Capture of Phobos and Deimos by Photoatmospheric Drag," *Icarus*, Vol. 37, No. 1, 1979, pp. 113–123.
https://doi.org/10.1016/0019-1035(79)90119-2

[2] Rosenblatt, P., Charnoz, S., Dunseath, K. M., Terao-Dunseath, M., Trinh, A., Hyodo, R., Genda, H., and Toupin, S., "Accretion of Phobos and Deimos in an Extended Debris Disc Stirred by Transient Moons," *Nature Geoscience*, Vol. 9, No. 8, 2016, pp. 581–583.
https://doi.org/10.1038/ngeo2742

[3] Fujimoto, M., "MMX (Phobos/Deimos Sample Return)," *16th Meeting of the NASA Small Bodies Assessment Group*, NASA Small Bodies Assessment Group, 2017.

[4] Sagdeev, R. Z., and Zakharov, A. V., "Brief History of the Phobos Mission," *Nature*, Vol. 341, No. 6243, 1989, pp. 581–585.
https://doi.org/10.1038/341581a0

[5] Marov, M., Avduevsky, V., Akim, E., Eneev, T., Kremnev, R., Kulikov, S., Pichkhadze, K., Popov, G., and Rogovsky, G., "Phobos-Grunt: Russian Sample Return Mission," *Advances in Space Research*, Vol. 33, No. 12, 2004, pp. 2276–2280.
https://doi.org/10.1016/S0273-1177(03)00515-5

[6] Cacciatore, F., and Martín, J., "Mission Analysis and Trajectory GNC for Phobos Proximity Phase of Phootprint Mission," *Advances in the Astronautical Sciences*, Vol. 153, 2015, pp. 1321–1340.

[7] Kawakatsu, Y., "Mission Design of Martian Moons Exploration (MMX)," *69th International Astronautical Congress*, International Astronautical Federation Paper 47632, 2018.

[8] Kogan, Y., "Distant Satellite Orbits in the Restricted Circular Three-Body Problem," *Cosmic Research (Translation of Kosmicheskie Issledovaniya)*, Vol. 26, June 1989, pp. 705–710.

[9] Hénon, M., "Numerical Exploration of the Restricted Problem. V. Hill's Case: Periodic Orbits and Their Stability," *Astronomy and Astrophysics*, Vol. 1, Feb. 1969, pp. 223–238.

[10] Benest, D., "Effects of the Mass Ratio on the Existence of Retrograde Satellites in the PCR3BP," *Astronomy and Astrophysics*, Vol. 45, No. 2, Dec. 1975, pp. 353–363.
https://doi.org/10.1017/CBO9781107415324.004

[11] Sidorenko, V. V., Neishtadt, A. I., Artemyev, A. V., and Zelenyi, L. M., "Quasi-Satellite Orbits in the General Context of Dynamics in the 1:1 Mean Motion Resonance: Perturbative Treatment," *Celestial Mechanics and Dynamical Astronomy*, Vol. 120, No. 2, 2014, p. 131–162.
https://doi.org/10.1007/s10569-014-9565-4

[12] Canalias, E., Lorda, L., and Laurent-Varin, J., "Design of Realistic Trajectories for the Exploration of Phobos," *2018 Space Flight Mechanics Meeting*, AIAA Paper 2018-0716, 2018.
https://doi.org/10.2514/6.2018-0716

[13] Laurent-Varin, J., "Preliminary Gravity Study for MMX Mission," CNES TR DYNVOL-NT-ORB/MOD-0738-CNES, Toulouse, France, Nov. 2017.

[14] Chen, H., Rambaux, N., Lainey, V., and Hestroffer, D., "Mothercraft-CubeSat Radio Measurement for Phobos Survey," *5th IAA Conference on University Satellites Missions and CubeSat Workshop*, GAUSS and International Academy of Astronautics Paper IAA-AAS-CU-20-05-09, 2020.

[15] Campagnola, S., Hernando-Ayuso, J., Kakihara, K., Kawabata, Y., Chikazawa, T., Funase, R., Ozaki, N., Baresi, N., Hashimoto, T., Kawakatsu, Y., Ikenaga, T., Oguri, K., and Oshima, K., "Mission Analysis for the EM-1 CubeSats EQUULEUS and OMOTENASHI," *IEEE Aerospace and Electronic Systems Magazine*, Vol. 34, No. 4, 2019, pp. 38–44.
https://doi.org/10.1109/MAES.2019.2916291

[16] Ikeda, H., Mitani, S., Mimasu, Y., Ono, G., Nigo, K., and Kwakatsu, Y., "Orbital Operations Strategy in the Vicinity of Phobos," *International Symposium on Space Flight Dynamics*, 2017.

[17] Wiesel, W. E., "Stable Orbits About the Martian Moons," *Journal of Guidance, Control, and Dynamics*, Vol. 16, No. 3, 1993, pp. 434–440.
https://doi.org/10.2514/3.21028

[18] Hénon, M., "Vertical Stability of Periodic Orbits in the Restricted Problem: II. Hill's Case," *Celestial Mechanics*, Vol. 8, No. 2, 1973, pp. 269–272.
https://doi.org/10.1007/BF01231427

[19] Robin, I. A., and Markellos, V. V., "Numerical Determination of Three-Dimensional Periodic Orbits Generated from Vertical Self-Resonant Satellite Orbits," *Celestial Mechanics*, Vol. 21, No. 4, 1980, pp. 395–434.
https://doi.org/10.1007/BF01231276

[20] Markellos, V. V., "Bifurcation of Planar to Three-Dimensional Periodic Orbits in the General Three-Body Problem," *Celestial Mechanics*, Vol. 25, No. 1, 1981, pp. 3–31.
https://doi.org/10.1007/BF01301803

[21] Lara, M., Russell, R. P., and Villac, B. F., "Classification of the Distant Stability Regions at Europa," *Journal of Guidance, Control, and Dynamics*, Vol. 30, No. 2, 2007, pp. 409–418.
https://doi.org/10.2514/1.22372

[22] Connor Howell, K., "Three-Dimensional, Periodic, 'Halo' Orbits," *Celestial Mechanics*, Vol. 32, No. 1, 1984, pp. 53–71.
https://doi.org/10.1007/BF01358403

[23] Koon, W. S., Lo, M. W., Marsden, J. E., and Ross, S. D., *Dynamical Systems, the Three-Body Problem and Space Mission Design*, Marsden Books, 2011, pp. 174–175.

[24] Russell, R. P., "Global Search for Planar and Three-Dimensional Periodic Orbits near Europa," *Advances in the Astronautical Sciences*, Vol. 54, No. 2, 2006, pp. 199–226.
https://doi.org/10.1007/BF03256483

[25] Doedel, E. J., Paffenroth, R. C., Keller, H. B., Dichmann, D. J., Galán-Vioque, J., and Vanderbauwhede, A., "Computation of Periodic Solutions of Conservative Systems with Application to the 3-Body Problem," *International Journal of Bifurcation and Chaos*, Vol. 13, No. 6, 2003, pp. 1353–1381.
https://doi.org/10.1142/S0218127403007291

[26] Chen, H., Canalias, E., Hestroffer, D., and Hou, X., "Stability Analysis of Three-Dimensional Quasi-Satellite Orbits Around Phobos," *69th*

International Astronautical Congress, International Astronautical Federation Paper 46646, 2018.

[27] Simo, C., "On the Analytical and Numerical Approximation of Invariant Manifolds," *Modern Methods in Celestial Mechanics*, edited by D. Benest, and C. Froeschle, Editions Frontieres, Gif-sur-Yvette, France, 1990, pp. 285–329.

[28] Pushparaj, N., Baresi, N., Ichinomiya, K., and Kawakatsu, Y., "Multi-Revolutional Periodic Orbit Transfers in the Ellipsoidal Gravity Field of Phobos," *International Symposium on Space Technology and Science*, Japan Soc. for Aeronautical and Space Sciences Paper 2019-d-022, 2019.

[29] Le Maistre, S., Rosenblatt, P., Rambaux, N., Castillo-Rogez, J. C., Dehant, V., and Marty, J. C., "Phobos Interior from Librations Determination Using Doppler and Star Tracker Measurements," *Planetary and Space Science*, Vol. 85, Sept. 2013, pp. 106–122.
https://doi.org/10.1016/j.pss.2013.06.015

[30] Rambaux, N., Castillo-Rogez, J. C., Le Maistre, S., and Rosenblatt, P., "Rotational Motion of Phobos," *Astronomy and Astrophysics*, Vol. 548, Dec. 2012, p. A14.
https://doi.org/10.1051/0004-6361/201219710

[31] Hénon, M., "Numerical Exploration of the Restricted Problem. VI. Hill's Case: Non-Periodic Orbits," *Astronomy and Astrophysics*, Vol. 9, Nov. 1970, pp. 24–36.
https://doi.org/10.1017/CBO9781107415324.004

[32] Lam, T., and Whiffen, G. J., "Exploration of Distant Retrograde Orbits Around Europa," *AAS/AIAA Space Flight Mechanics Meeting*, American Astronautical Soc. Paper 05-110, 2005.

[33] Chen, H., Canalias, E., Hestroffer, D., and Hou, X., "Sensitivity Analysis and Stationkeeping of Three-Dimensional Quasi-Satellite Orbits around Phobos," *32nd International Symposium on Space Technology and Science*, Japan Soc. for Aeronautical and Space Sciences Paper 2019-d-063, 2019.

[34] Asphaug, E., and Melosh, H., "The Stickney Impact of Phobos: A Dynamical Model," *Icarus*, Vol. 101, No. 1, 1993, pp. 144–164.
https://doi.org/10.1006/icar.1993.1012

[35] Kozai, Y., "The Motion of a Close Earth Satellite," *Astronomical Journal*, Vol. 64, Nov. 1959, pp. 367–377.
https://doi.org/10.1086/107957